ABSTRACT

PRABHU, SANTOSH. A Two-Dimensional Finite Element Model of Electron Beam Additive Manufacturing. (Under the direction of Dr. John S Strenkowski)

A two-dimensional finite element model of electron beam additive manufacturing was developed using ANSYS Parametric Design Language (APDL) to assess part distortion as a function of the process parameters – beam power, beam speed and dwell time. The two-dimensional model incorporates a coupled thermal and mechanical simulation with radiation and convection. Temperature dependent material properties were incorporated into the model. The moving heat source was described as a Gaussian distribution. The birth death technique was employed to simulate realistically the addition of material as multiple layers. The beam power, speed and dwell time were varied over a range and different combinations of these parameter values were used to run a total of 48 test cases using the two-dimensional model. The model simulated distortion as a function of the various additive manufacturing process parameters. The distortion was expected to increase with increase of beam power and the model confirmed it. Variation of dwell time and beam speed showed a trend of decreased distortion with an increase of these parameters. Based on these results, the model suggests that the process parameters need to be appropriately considered before a part is built.

A Two-Dimensional Finite Element Model of Electron Beam Additive Manufacturing

by
Santosh Prabhu

A thesis submitted to the Graduate Faculty of
North Carolina State University
in partial fulfillment of the
requirements for the Degree of
Master of Science

Mechanical Engineering

Raleigh, North Carolina

2017

APPROVED BY:

Dr. Hsiao-Ying Shadow Huang

Dr. Mark Pankow

Dr. John S Strenkowski
Committee Chair

DEDICATION

To my family who have always stood by me.

BIOGRAPHY

Santosh Prabhu was born in Bangalore (in the state of Karnataka), India in 1989. He completed his B.E. in Mechanical Engineering from Rashtreeya Vidyalaya College of Engineering, Viswesvaraiah Technological University, Bangalore in 2011. Post graduation, he entered the industry and started his career as a Design Engineer with the Research and Development unit of Mercedes Benz in India. He is currently pursuing a Masters of Science in Mechanical Engineering at NC State.

ACKNOWLEDGMENTS

I would like to thank my family, friends, advisor and colleagues for helping me achieve this.

TABLE OF CONTENTS

LIST OF TABLES

LIST OF FIGURES

1 INTRODUCTION

1.1 Background

The Industrial Revolution was responsible for the transition from hand production methods of parts to machines producing them. This created a demand for metal parts in machinery which led to the development of machine tools like the lathe, drilling and milling machines. A part manufactured using these machines involved material being removed from a billet or stock part to achieve its final shape. This type of "subtractive manufacturing" has been responsible for most of the metal parts we use in today's world.

Additive Manufacturing (AM) is a new technology that was developed in the late 1980s that involved building a three-dimensional object from nothing as opposed to conventional metal removal processes. It involves building a part by adding material in layers, each layer being a thin cross-section of the part derived from a digital Computer-Aided Design (CAD) file. The parts can be of any shape, geometry and complexity and are typically built in a single stage. The different additive manufacturing processes that are available today differ in the materials that can be used, how the layers are created, and how the layers are bonded to each other. These differences determine factors like the accuracy, material and mechanical properties of the final part. They also determine factors like how quickly the part can be made, how much post-processing is required, the size of the AM machine used, and the overall cost of the machine and process. Additive manufacturing is already used to make some niche items, such as medical implants, and to produce plastic prototypes for engineers and designers.

Electron Beam Additive Manufacturing (EBAM) is an AM process for metal parts, that utilizes an electron beam as a heat source. In this process, near net shape components are fabricated in a layer-by-layer manner directly from digital CAD files. It allows different part geometries, on the scale of mm^3 to m^3, to be created. Each layer is formed by melting individual passes from a wire or powder material in a high vacuum, which undergoes rapid heating, melting, solidification, and cooling during the deposition process to produce fully dense parts. The powder feedstock is typically an alloy like titanium alloys (Ti6Al4V), inconel, cobalt alloys, nickel alloys and copper nickel alloys.

As the part is fabricated, the deposited material undergoes repeated heating and cooling cycles as more passes and layers are added. This results in a temperature gradient being induced between layers. One of the consequences of these induced thermal gradients is the build-up of undesirable levels of distortion and residual stress. This unwanted distortion and residual stress can lead to loss of tolerance and failure. Currently these issues are dealt with using an experimental trial and error approach where several samples are manufactured to iteratively reach the desired outcome. In addition to being time consuming and expensive, the trial and error approach yields little understanding pertaining to distortion and residual stress mitigation, as even slight changes to the build plan can result in large changes in distortion and stress accumulation. A predictive model will be of immense help in helping reduce these distortions and stresses in the final part. From this model, we will also be able to learn how the various process parameters contribute to the distortion of parts and the formation of residual stresses.

Armed with this information, we can predict beforehand the process plan that will need to be implemented to obtain parts with minimum distortion and residual stresses.

1.2 Research Objective

The objective of this work is to develop a finite element model of a moving heat source that will produce thermo-mechanical simulations of AM processes. This model can be used as a tool to predict the effect of process parameters in building parts using EBAM, to reduce the amount of distortion in the built parts. This finite element model will predict temperature history and distortion of the part during the build as well as post process distortion. The optimal process parameters of beam power, beam speed and dwell time can then be identified for a given shape or geometry.

2 LITERATURE REVIEW

The use of finite element modeling (FEM) of AM to predict distortion and residual stress originates from prior research performed in the field of welding. Multi-pass welding is a similar process to AM, in that a heat source is used to melt material on to a workpiece where it is allowed to cool and solidify. Like in AM, thermal gradients lead to unwanted distortion and residual stress. Due to the fact that welding and AM processes share many similarities, the numerical models are also comparable.

2.1 Moving Heat Source

The research activity in welding simulation started decades ago. Rosenthal [1] was among the first researchers to develop an analytical solution of heat flow during welding based on conduction heat transfer for predicting the shape of the weld pool for two and three-dimensional welds. Using the Fourier partial differential equation (PDE) of heat conduction, he introduced the moving coordinate system to develop solutions for the point and line heat sources and applied this successfully to address a wide range of welding problems. His analytical solutions of the heat flow made possible for the first time the analysis of the process from a consideration of the welding parameters namely the current, voltage, welding speed, and weld geometry.

Since the pioneering work of Rosenthal, Friedman [2] proposed to apply the Gaussian distributed heat source to approximately express the heat flux at the heating spot. Goldak et al.

[3] took this one step further. They developed a mathematical model for welding heat sources based on a Gaussian distribution and proposed two models, a semi-ellipsoidal and double ellipsoidal distribution in order to capture the size and shape of the heat source for shallow and deeper penetrations.

N.T.Nguyen et al. [4] developed analytical solutions for the transient temperature field of a semi-infinite body subjected to 3D power density moving heat sources (such as semi-ellipsoidal and double ellipsoidal heat sources) and were experimentally validated. It was shown that the analytical solution obtained for double ellipsoidal heat source was a general solution that can be reduced to semi-ellipsoidal, semi-sphere, 2D Gaussian-distributed heat source and the classical instant point heat source.

2.2 Laser Based Processes

A large amount of work has been carried out in the field of laser based AM processes. Deus and Mazumdar [5] developed 3D transient thermal and mechanical Lagrangian FE models, consistent with the additive nature of the process, using the Abaqus™ software package. Temperature and residual stress profiles were calculated, for cladding of C95600 copper on AA333 aluminum-alloy. These models were useful in investigating the range of processing parameters that lead to successful deposition.

Toyserkani et al. [6, 7] proposed a 3D transient finite element model of laser cladding by powder injection to investigate the effects of laser pulse shaping on the process. The proposed model could predict the clad geometry as a function of time and process parameters including laser pulse shaping, travel velocity, laser pulse energy, powder jet geometry, and material properties. The quality of clad bead for different parameter sets was experimentally evaluated and shown as a function of effective powder deposition density and effective energy density.

Contuzzi et al. [7] evaluated the influence of process parameters on the temperature evolution in a 3D model built using Selective Laser Melting (SLM). The developed code evaluated the distribution and evolution of the temperatures in the SLM process and simulated the powder-liquid-solid change by means of a check of the nodes temperature.

Picasso et al. [8] proposed a model which took into account the main phenomena occurring during the laser-cladding process. For a given laser power, beam radius, powder jet geometry, and clad height, the model evaluated two other processing parameters, namely, the laser beam velocity and the powder feed rate. It considered the interactions between the powder particles, the laser beam, and the molten pool. The melt-pool shape was computed using a 3D analytical model. The predictions obtained with this numerical model were in good agreement with experimental results.

Weerasinghe and Steen [9] developed a 3D finite difference model to calculate the clad weld bead dimensions and temperature distribution in the heating zone in laser cladding.

Hoadley and Rappaz [10] proposed a 2D finite element model for laser cladding by powder injection. The model simulated the quasi-steady temperature field for the longitudinal section of a clad track. It took into account the melting of the powder in the liquid pool and the liquid gas free surface shape and position. The calculated clad heights agreed well with the experimental values for the conditions where a cobalt-based hard-facing alloy is clad onto mild steel with a linearly focused laser source.

Zhao et al. [11] developed a 3D finite element model for precisely simulating the laser cladding process with a focus on dilution control. Dilution refers to the contamination level of the properties of clad layer by substrate metals. They developed and verified a Lagrangian finite element method with the help of experiments and quantitatively addressed the effects of process parameters on the dilution of clad layer.

Kar and Mazumder [12] proposed a mathematical model to determine the composition of metastable alloys and to study the effects of various process parameters on the composition of extended solid solution in the cladding alloys of Ni-Al. The model also determined the effect of process parameters on the composition of the alloy.

Vasinonta et al. [13] presented thermomechanical models for the building of thin-walled structures by laser-based Solid Freeform Fabrication (SFF) processes that helped quantify the effects of changes in wall height, laser power, deposition speed and part preheating on melt pool size (for consistent build conditions) and thermal gradients (for limiting residual stresses). Mechanical simulations were used to demonstrate the link between thermal gradients and maximum final residual stresses. These models were applied to the Laser Engineered Net Shaping (LENS) process; however, the general approach, insights and conclusions are applicable to most SFF processes involving a moving heat source. Results from the residual stress simulations also identified mechanisms for reducing residual stresses and quantified maximum stress reductions that can be achieved through manipulation of all process variables.

Nickel et al. [14] studied the effect of deposition patterns on the resulting stresses and deflections in laser deposited metal parts. Finite element modeling of the deposition processes showed that the deposition pattern has a significant effect on the part stresses and deflections. In their study, they found that for a beam geometry, a raster pattern with lines oriented 90 degrees from the beam's long axis produced the lowest deflections. For a plate geometry, the spiral pattern scanned from the outside to the inside produced low and uniform deflections.

Labudovic et al. [15] developed a 3D finite element model of the heat flow and residual stresses in a direct laser metal powder deposition process. The simulation results provided the cross-sectional shape of the molten pool which were in good agreement with experimental data. Modeling results of residual stress calculations were confirmed by x-ray diffraction residual stress measurements and they found that cracking can be avoided by preheating the specimen. The cracking can also be avoided by stress relieving which significantly reduces the residual tensile stress level.

N’Dri et al. [16] developed micro and macro models to capture physical processes of Direct Metal Laser Sintering (DMLS) processes including melt pool dynamics, shape of solidified tracks, as built residual stresses and distortions. The models were verified and partially validated by comparing numerical predictions with experimental observations and measurements. For the build of a cube specimen, they found that rotating the deposit starting point by 90 degrees for each new layer significantly reduced the distortion of the final part.

Cottam et al. [17] investigated the effect of deposition rate on the residual stresses formed during the laser cladding of Ti6Al4V powder on to a Ti6Al4V substrate. An analytical cladding model was used to control the depth of the melt pool and clad height during the laser cladding to determine the influence of deposition rate on the development of residual stresses. The microstructures were found to be consistent with all the samples investigated, as was the residual stress distribution and magnitude, which led to the conclusion that the development of residual stress is independent of the deposition rate when cladding Ti6Al4V powder on to a Ti6Al4V substrate.

Roberts et al. [18] developed an innovative 3D thermal-elasto-plastic finite element model for predicting the deformation and residual stresses in Ti6Al4V parts built on steel platforms. The developed model utilized temperature dependent material physical and mechanical properties as well as latent heat of melting. Surface profilometry showed good agreement with the simulation results and they found that as the number of layers in the part increases, the platform deformation and the surface residual stresses also increase. They also found that with decrease in thickness of the platform, the platform distortion increases.

Matsumoto et al. [19] proposed a method for calculating the distribution of temperature and stress within a single metallic layer formed on the powder bed in the selective laser melting method. The solidified layer was assumed to be subjected to plane stress deformation and the 2D finite element methods for heat conduction and elastic deformation were combined. They found that the amount of the deflection of the solid layer increased as the track length increased. In order to prevent the distortion of the solid layer on the powder bed, it is desirable to shorten the scanning track. When the neighbouring track began to solidify, a large tensile stress between the solidified tracks appeared at the side end of the solid part, which may cause the cracking of the layer. They also suggested dividing large scan areas into smaller areas and then using short scanning tracks to scan these areas to reduce the possibility of cracking.

Moser et al. [20] developed a finite volume model to predict the temperature and melt percentage of a multiple layer part build using the Selective Laser Sintering (SLS) process. They demonstrated how the model may be used to predict melt percentage and thus, the final form, along with any defects. If scaled up, the model has the potential to aid in the development of improved SLS laser scan patterns as well as to provide the ability to predict defects in a part produced using a given scan pattern.

Cheng [21] conducted finite element simulation for the fabrication of a TC15 titanium alloy brick part using laser powder deposition, which involved a multilayer and multitrack deposition process directed by the manoeuvring of a laser beam. The simulation entailed modelling of the brick part by employing the 'birth and death' technique and of the laser beam as a moving heat flux. The thermal stress was found to be much stronger perpendicular to the scanning direction due to larger temperature gradient, and the Von Mises stress resided mainly in the center of the top layer and along the circumferences of intermediate layers easily leading to fractures perpendicular to and parallel to the deposition surface respectively. Scanning along the long edge direction led to much smaller stress, thus better quality, compared with scanning along the short edge direction, while in terms of stress there was little difference between unidirectional and back-and-forth scanning.

Mercelis and Kruth [22] developed a simple theoretical model to predict residual stress distributions in Selective Laser Sintering (SLS) and Selective Laser Melting (SLM) and conducted experiments to measure residual stress profiles in a set of test samples produced with different process parameters. The residual stress profile was found to consist of two zones of large tensile stresses at the top and bottom of the part, and a large zone of intermediate compressive stress in between. The most important parameters determining the magnitude and shape of the residual stress profiles were the material properties, the sample and substrate height, the laser scanning strategy and the heating conditions.

Dai and Shaw [23] carried out 3D finite element modeling to investigate the temperature field in the processing of multiple material components using a moving laser beam. Transient and residual stresses as well as distortion of the component were also analyzed. Effects of laser processing conditions such as fabrication sequences, laser scanning patterns and scanning rates were investigated and found that the temperature distribution, transient stress, residual stress and distortion of a multi-material component are dependent on the laser processing conditions as well as the material properties, especially the thermal conductivity and coefficient of thermal expansion. They found that fabricating the section of the high melting temperature material first and then the section of the low melting temperature material was the appropriate sequence to fabricate the part made of two materials with substantially different melting points. This resulted in relatively small thermal stresses in the final part.

Li et al. [24] developed a practical finite element model for fast prediction of part distortion in SLM. The predicted distortions in four different scanning strategies were investigated and verified by the experimental data. The predicted part distortions showed that the horizontal scanning pattern produced the smallest deflection along longitudinal direction and the biggest deflection along crosswise direction. On the contrary, the vertical scanning pattern resulted in the biggest deflection along longitudinal direction and smallest deflection along crosswise direction. The successive scanning strategy is preferred to the least heat influence pattern in terms of reducing part distortion.

Buchbinder et al. [25] investigated the effects of preheating during SLM of aluminium components and determined an appropriate preheating temperature at which distortion practically no longer occurs. A significant reduction in distortion compared to the distortion without preheating was experienced beginning at a preheating temperature of 150 degree Celsius. At a preheating temperature of 250 degree Celsius, distortion was no longer detected, thereby concluding that a preheating temperature of 250 degree Celsius is suitable for reliably manufacturing parts made out of AlSi10Mg using SLM.

Paul et al. [26] developed a 3D thermomechanical finite element model which calculated the thermal deformation in AM parts based on slice thickness, part orientation, scanning speed, and material properties. The thermal deformation model was then superimposed with a geometric virtual manufacturing model of the AM process to calculate the form and runout errors in AM parts. General trends were observed between the errors and part orientation and slice thickness that will allow practitioners to appropriately select the orientation and slice thickness that will satisfy the design GD&T specifications of the part.

Marimuthu et al. [27] investigated the prediction of the distortion generated in an aero-engine component produced by the direct laser deposition process through finite element analysis. They found that substrate distortion can be minimised by increasing the substrate thickness. The clad deposition pattern had significant impact on substrate distortion. Depositing from outside to inside showed lower distortion than from inside to outside. Tool path and tool path start position was found to be a key process variable which can influence the substrate distortion.

Papadakis et al. [28] utilized a heat input reduction model to estimate the shape distortion and component behaviour after it has been detached from the supports and the substrate. The study found that there is a complex relation between part thickness and total heat input and that the final part distortion is based on an equilibrium being reached by these two parameters.

2.3 Electron Beam Processes

Yan et al. [29] analyzed the process of depositing stiffeners on a flat plate by electron beam freeform fabrication (EBF) by uncoupled thermal–mechanical finite element (FE) simulation. The deposition of the stiffeners was realized by two steps: (1) stiffeners were deposited on the positive side of the panel and cooled to room temperature and (2) stiffeners were deposited on the reverse side of the panel and cooled to room temperature. The simulation results showed that the warping direction of the panel is opposite to the stacking direction of the stiffeners.

Denlinger et al. [30] developed a finite element modeling strategy to allow for the prediction of distortion accumulation in large workpieces in AM. They performed a 3D Lagrangian thermoelastoplastic analysis using a combined hybrid quiet inactive element activation strategy with adaptive coarsening. The effectiveness of the modeling strategy was demonstrated and experimentally validated on a large electron beam deposited Ti6Al4V part consisting of 107 deposition layers. Model validation using experimental measurements showed that the proposed strategy can accurately predict the distortion of AM large parts. It could also determine which deposition passes were responsible for the majority of the substrate distortion, which is important in designing process plans that mitigate distortion.

Cheng et al. [31] developed a 3D thermos-mechanical model for temperature and stress prediction in EBAM, particularly, in overhang features. They found that the poor thermal conductivity of Ti6Al4V results in higher temperatures in overhang builds due to slower heat dissipation. These retained higher temperatures result in higher residual stresses after cooling. A smaller porosity of the powder used to build the overhang may help reduce the thermal stresses.

Lacki and Adamus [32] simulated electron beam welding of tubes. The numerical calculation took into consideration thermomechanical coupling and allowed for the optimization of the process parameters such as welding speed, power of the heat source and shape of the joint before welding. The study revealed that higher temperature gradients in the part resulted in higher effective stresses.

Denlinger et al. [33] developed a finite element model for predicting the thermo-mechanical response of Ti-6Al-4V during electron beam deposition. A three-dimensional thermo-elasto-plastic analysis was performed to model distortion and residual stress in the part and experimental in situ temperature, and distortion measurements are performed during the deposition of a single-bead-wide, 16-layer-high wall built for model validation. The in situ distortion and post-process residual stress measurements suggested that stress relaxation occurs during the deposition of Ti-6Al-4V. A method of accounting for such stress relaxation in thermo-elasto-plastic simulations was proposed where both stress and plastic strain was reset to zero, when the temperature exceeds a prescribed stress relaxation temperature.

Shen and Chou [34] proposed a coupled thermomechanical finite element model to simulate the transient heat transfer, part residual stresses of alternate raster scan during the EBAM process subject to a moving heat source with a Gaussian volumetric distribution. The coupled mechanical simulation was able to capture the evolution of the part residual stresses in EBAM. It was found that the peak temperature was 100 degree Celsius higher for the alternate raster scan when compared to the single straight scan. Tensile residual stress was always found to be present in the final cooled parts due to the contraction and the compressive stress extends deeper into the substrate, even to the bottom, for both single straight scan and multi-layer alternate raster scan.

Zah et al. [35] developed a thermal simulation model by the formulation of a mathematically abstracted heat source, based on the general heat conduction equation with a moving energy source. Various combinations of process parameters were applied within the simulation in order to determine the temperature as well as the size and shape of the melt pool. The results were compared with real experiments and it was found that these results concur largely with the simulation. In the future, experimental simulation series can be conducted before the actual build-up of the parts in order to investigate the correct values of the applied parameters.

2.4 Other AM Processes

Klingbeil et al. [36] conducted warping experiments on plate-shaped specimens created by microcasting and welding processes used in Shape Deposition Manufacturing (SDM). Results from the experiments and numerical models suggested that a combination of initial substrate preheating and part insulation can be applied to SDM and similar SFF processes to limit warping deflection.

Turner and Gold [37] critically reviewed the literature related to dimensional accuracy and surface roughness for fused deposition modeling and similar extrusion-based additive manufacturing. They found that fused deposition modelling and related processes are the most widely used polymer rapid prototyping processes. For many applications, resolution, dimensional accuracy and surface roughness are among the most important properties in final parts. Thermal warping and shrinkage are often major sources of dimensional error in finished parts. Product design parameters, in particular, slice height, strongly impact surface roughness.

3 MODEL AND VALIDATION

3.1 Theory of Heat Transfer

Electron Beam Additive Manufacturing (EBAM) involves local heating of material to high temperatures followed by rapid cooling. During this process, the various thermal and mechanical properties of the material vary with temperature and these variations are not always linear. Thus, the simulation of this process is a nonlinear transient heat transfer analysis. The governing heat transfer energy balance equation is written as:

$$\rho C_p \frac{dT}{dt} = -\nabla \cdot q(r,t) + Q(r,t)$$

where ρ is the material density, C_p is the specific heat capacity, T is the temperature, t is the time, Q is the heat source, r is the relative reference coordinate, and q is the heat flux vector, calculated as:

$$q = -k\nabla T$$

where k is the thermal conductivity. The above heat transfer energy balance equation is the differential equation of heat conduction for a stationary homogenous isotropic solid.

Two other heat transfer mechanisms that may play a role during the process are convection and radiation. Thermal radiation is accounted for using Stefan Boltzmann's law given by:

$$q_{rad} = \varepsilon\sigma\left({T_s}^4 - {T_\infty}^4\right)$$

where ε is the surface emissivity, σ is the Stefan-Boltzmann constant, T_s is the surface temperature of the workpiece and T_∞ is the ambient temperature (25 °C).

Convection is governed by Newton’s law of cooling given by:

$$q_{conv} = h(T_s - T_\infty)$$

where h is the convection film coefficient.

The moving heat source is described by Goldak’s [3] semi-ellipsoidal heat source in which heat flux is distributed in a Gaussian manner throughout the heat source’s volume and is given by :

$$q(x, y, z) = \frac{6\sqrt{3}Q}{abc\pi\sqrt{\pi}} e^{\left(-\frac{3x^2}{a^2} - \frac{3y^2}{b^2} - \frac{3z^2}{c^2}\right)}$$

where Q is the input heat source and a,b,c are the semi-axes of the ellipsoid. This heat source distribution is reduced to two dimensions to suit the current model and is given by :

$$q(x, y) = \frac{3Q}{\pi ab} e^{\left(-\frac{3x^2}{a^2} - \frac{3y^2}{b^2}\right)}$$

3.2 Material Properties

The material being considered for the simulation is a titanium alloy, Ti6Al4V. The material properties of metals, for instance, the specific heat capacity, thermal conductivity, modulus of elasticity and yield stress, vary with temperature and these variations need to be considered during the simulation to get accurate results. The following table (Table 1) lists the various thermal and mechanical properties for Ti6Al4V. The properties have been obtained by extensive research into material property handbooks [38-41] and the literature of previous researchers [42].

Table 1: Material properties of Ti6Al4V

Temperature (^oC)	Density (kg/m^3)	Specific Heat Capacity Cp (J/K/kg)	Thermal Conductivity k (W/m/K)	Coefficient of thermal expansion α (μm/m/^oC)	Modulus of Elasticity E (GPa)	Yield Strength (MPa)	Poisson's Ratio
25	4430	565	6.60	8.60	104.00	768	0.34
93		565	7.30	8.70	101.00	735	
250		586	9.72	9.20	91.81	665	
500		682	13.92	9.70	78.63	552	
800		714	17.50	9.70	62.80	417	
1650		759	28.40	9.70	1.04	8	

3.3 Finite Element PLANE13

The finite element simulation was carried out in ANSYS using ANSYS Parametric Design Language (APDL) module. Within ANSYS, there are three ways to perform a thermal stress or strain analysis – a single stress analysis with directly applied temperatures, separate thermal and stress analysis run in series and single analysis using coupled or multi-field elements. If the temperature loading is known, the first method is used with the temperatures being applied as body loads. In most cases, however, the complete temperature loading is not known and a thermal analysis may need to be performed to determine the temperature distribution, possibly varying over time. In the second method, a thermal analysis is first performed to obtain the nodal temperature solution. These nodal temperature loads are then applied as body loads to a separate structural analysis. However, compatibility between the thermal and structural models in terms of whether they have the same mesh needs to be checked. For example, in a thermal analysis, it may not be necessary to model small details such as fillets, and a relatively coarse mesh is sufficient to capture the temperature gradients.

In the structural analysis, however, fillets are often critical areas of stress concentration and a finer mesh may be needed throughout the model. In the third method, a multi-field element which has both temperature and displacement degrees of freedom is used in an iterative analysis to obtain the coupled thermal and structural solutions at the same time. This method is more computationally efficient and has been considered in the current model.

The simulation is a two-dimensional coupled field analysis. A coupled-field analysis is a combination of analyses from different engineering disciplines that interact to solve a global engineering problem, hence, a coupled-field analysis is often referred to as a multiphysics analysis. When the input of one field analysis depends on the results from another analysis, the analyses are coupled. In this coupled analysis, the PLANE13 element has been used. PLANE13 has a 2-D magnetic, thermal, electrical, piezoelectric, and structural field capability with coupling between the fields. PLANE13 is defined by four nodes with up to four degrees of freedom per node. In the current simulation, the PLANE13 element has been limited to the structural-thermal field coupling.

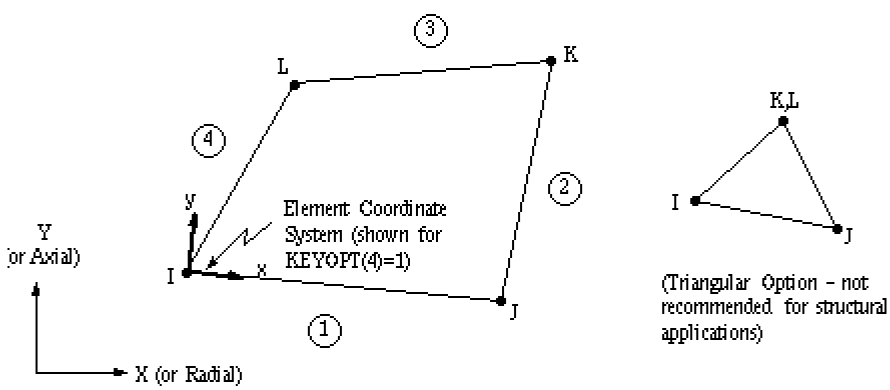

Figure 1: PLANE13 2-D Coupled-Field Solid

3.4 Plasticity Options

During the course of a nonlinear material analysis, a number of material-related factors can cause the structure's stiffness to change. Nonlinear stress-strain relationships of plastic, multilinear elastic and hyperelastic materials will cause a structure's stiffness to change at different load levels and at different temperatures. Creep, viscoplasticity and viscoelasticity will give rise to nonlinearities that can be time-, rate-, temperature-, and stress-related. Any of these kinds of material properties can be incorporated into an ANSYS analysis by using appropriate plasticity options that are available in ANSYS.

The various options available in ANSYS to describe plastic behavior are:

1.) Bilinear Kinematic Hardening
2.) Multilinear Kinematic hardening
3.) Bilinear Isotropic Hardening
4.) Multilinear Isotropic Hardening
5.) Nonlinear Elasticity
6.) Anisotropic

The hardening rule describes how the yield surface changes (size, center, shape) as a result of plastic deformation. In kinematic hardening, the yield surface remains constant in size and translates in the direction of yielding. In isotropic hardening, the yield surface expands uniformly in all directions with plastic flow. Bilinear models assume a fixed tangent modulus in the plastic regime. Multilinear discretizes the plastic region into a number of linear portions, each having its own tangent modulus. Anisotropic is described by the uniaxial tensile and compressive stress-strain curves in three orthogonal directions and the shear stress-engineering shear strain curves in the corresponding directions.

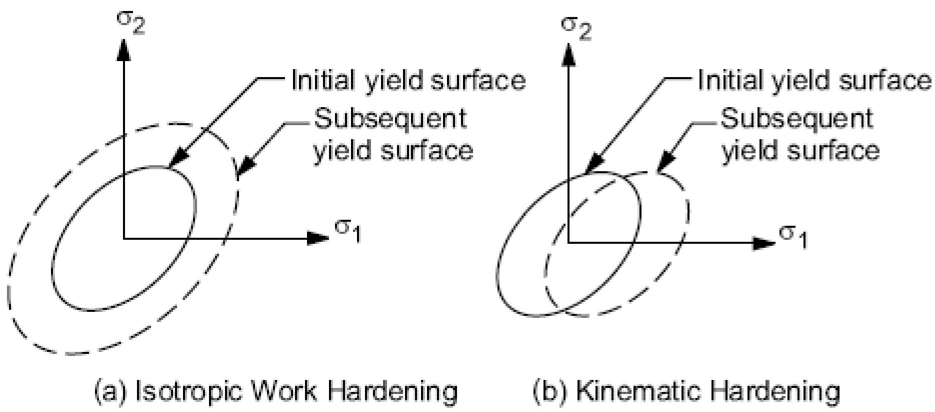

Figure 2: Kinematic and Isotropic Hardening

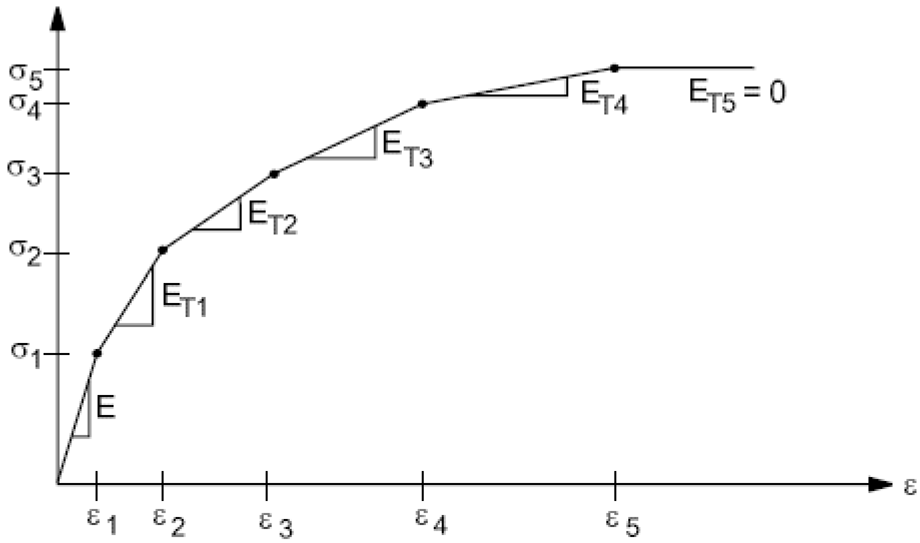

Figure 3: Multilinear Hardening

Using these options, the plastic behavior of the material beyond the elastic limit and at different temperatures can be defined. However, in order to do so, either the stress and strain data points or tangent moduli beyond the point of yield is required to accurately describe the stress-strain curve. For the case of Ti6Al4V in the current model, the material properties up to a temperature of 800^{o}C has been defined, but the stress and corresponding strain values beyond the yield point are currently not available in the literature. Additionally, it is not recommended to use the Bilinear Kinematic Hardening in large strain applications. As a result, the Bilinear Isotropic Hardening has been considered in the plastic regime in the simulation and a value of 10% of the modulus of elasticity has been assumed for the tangent modulus.

3.5 Model Validation

Before the simulation was performed, the heat source model was validated against previous work done by Chen [43]. In that study, the temperature fields and distortions induced in steel plates due to welding had been researched. The temperature distribution over time were compared with the results obtained by Chen to validate the model. The plate had dimensions of 300 x 130 x 6 mm with a heat source input of 5350W moving at a speed of 6mm/s. The temperature contours at different time intervals are given in the following two pages for both the current model and Chen's model.

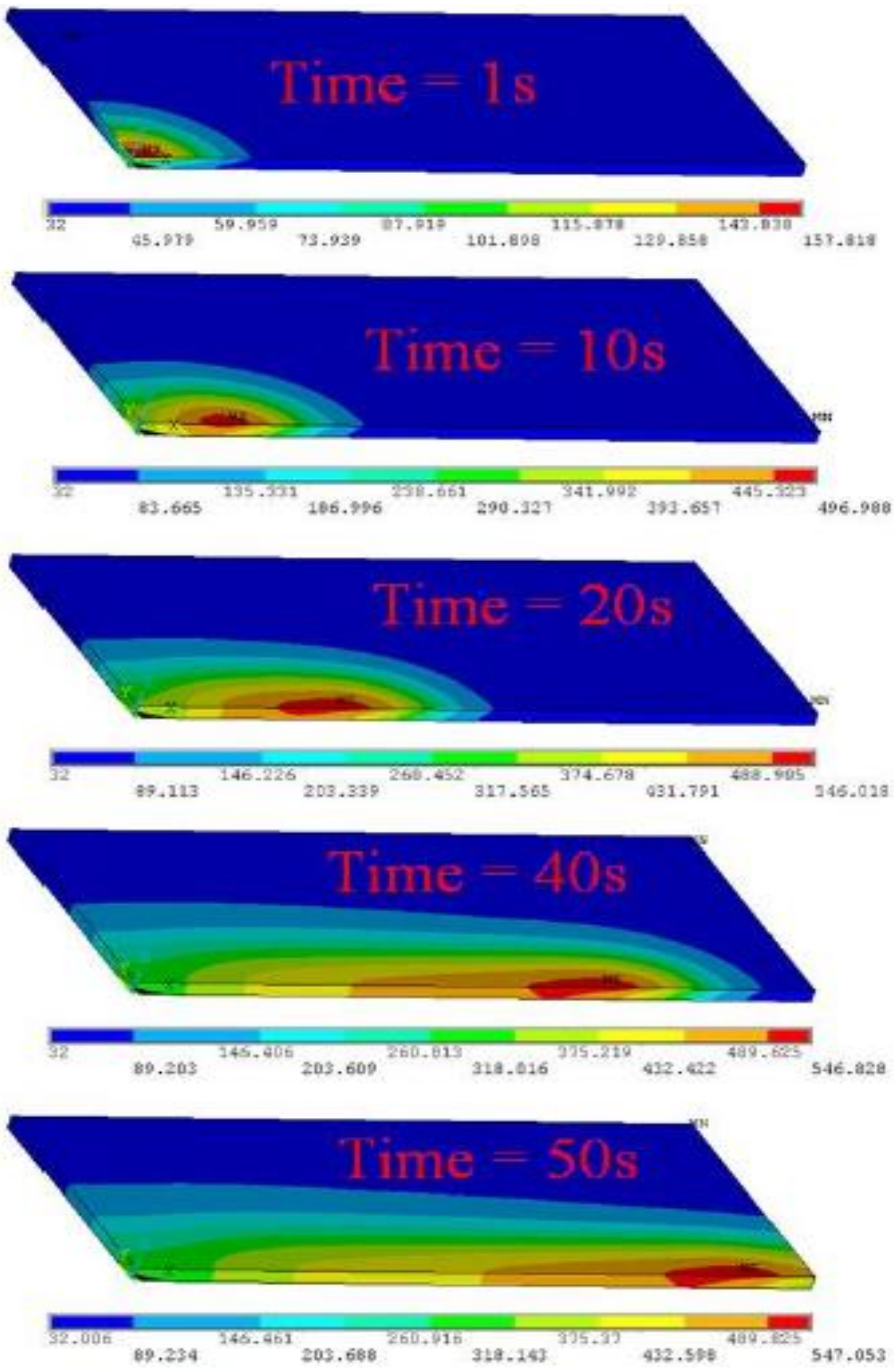

Figure 4: Temperature distribution during welding - Chen [43]

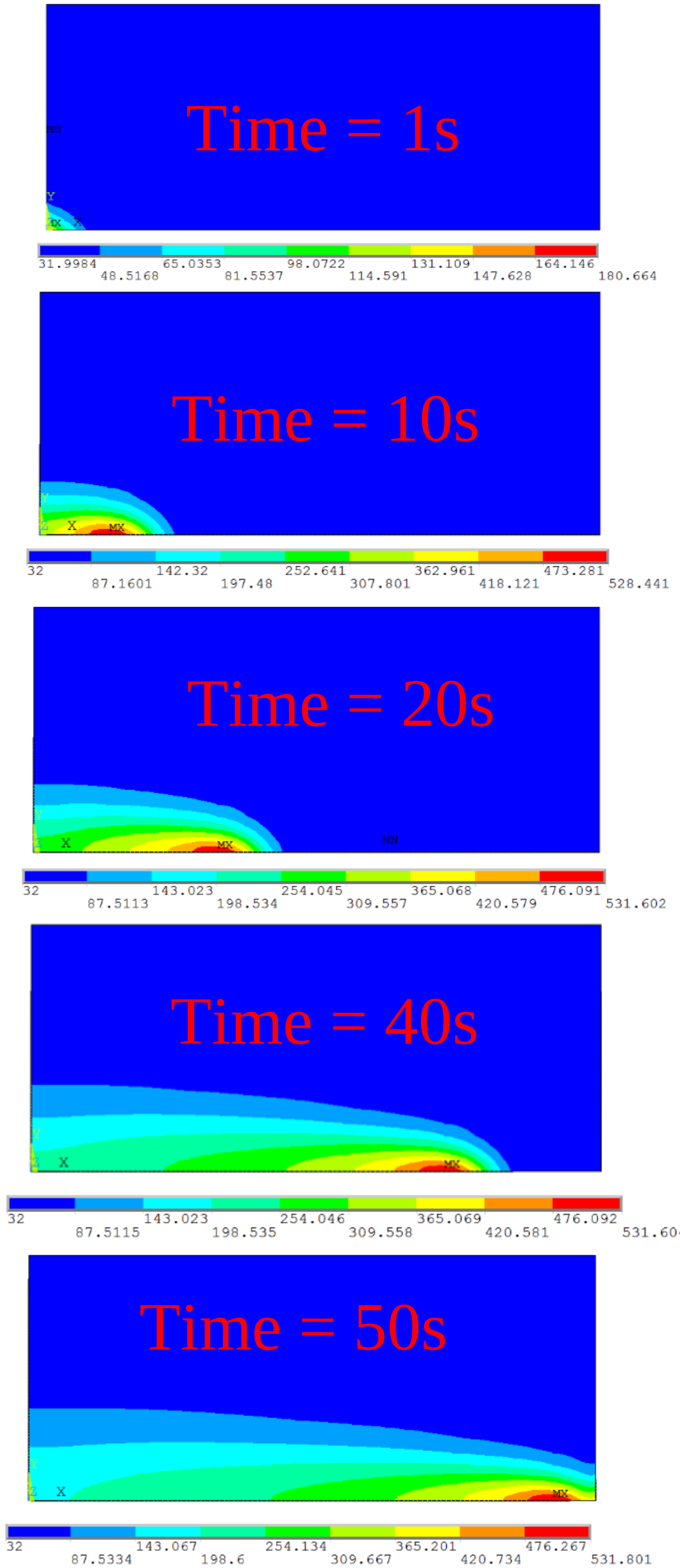

Figure 5: Temperature distribution during welding – current model

The temperature contours obtained by using Chen's model's dimensions and heat source input compare favorably to a large extent to his results. The maximum temperature that is reached in the current model is 532°C. When compared with his model's maximum temperature of 547°C, the error was found to be within 3%. In this manner, the heat source model was validated.

In addition to the above validation, the model was compared with the analytical solution for the Timoshenko beam with a fixed support at one end and a roller support at the other end, whose top and bottom fibers are subjected to two different temperatures.

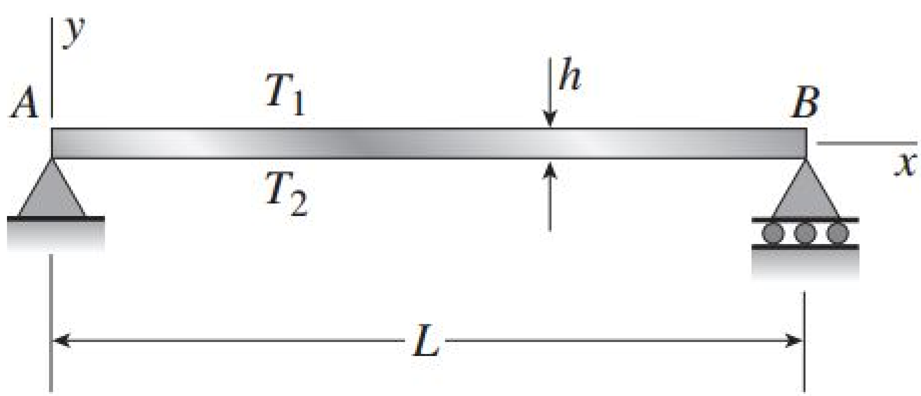

Figure 6: Timoshenko beam [45]

The analytical solution for the deflection for the beam is given by:

$$v = -\frac{\alpha(T_2 - T_1)(x)(L - x)}{2h}$$

where α is the coefficient of thermal expansion of the beam. Consider a case where the material of the beam is Ti6Al4V. Its length is 250 mm and its height is 10 mm. T_1 is 100°C and T_2 is 200°C. For this configuration and using the average thermal expansion coefficient value of $9.0*10^{-6}$ from Table 1, the deflection at the midspan from the analytical solution was found to be 0.7109 mm. Using these same properties and beam dimensions, the simulation was carried out in ANSYS using the PLANE13 element and assuming a plane stress condition. The deflection obtained in ANSYS at the midspan was 0.66725 mm, giving an error of about 6%. These favorable results from the heat source model and beam deflection model helped validate the current approach. The results of these simulations are covered in the next chapter.

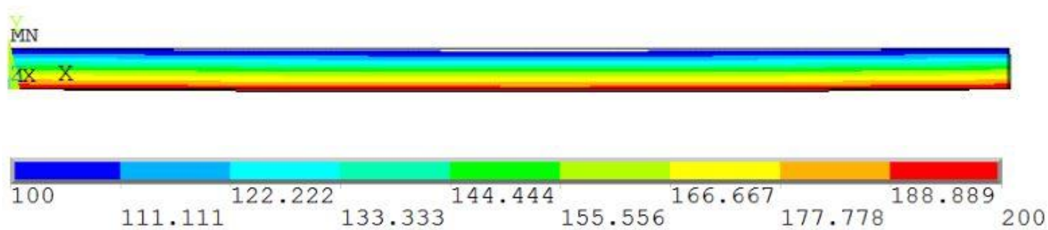

Figure 7: Temperature distribution in ANSYS

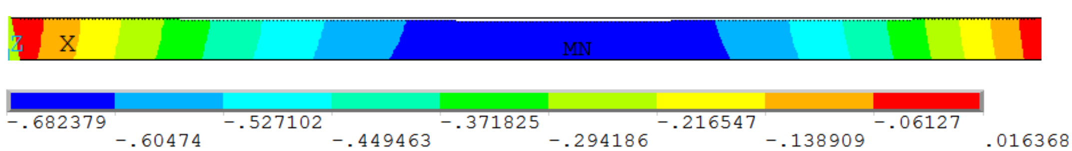

Figure 8: Deflection in ANSYS

4 RESULTS AND DISCUSSION

4.1 Model and Results

A two-dimensional model is considered in the current simulation. It consists of a base or a substrate, made of the same material as the final part (Ti6Al4V), which is 254 mm in length and 12.7 mm in height. The build will occur on this substrate. The part being manufactured is a solid plate which is 203.2 mm in length and 48 mm in height. This height was sliced into 16 layers for the current simulation. The mesh model had a total of 3460 elements. The entire model was constrained in the vertical or Y direction at the ends and constrained in the horizontal or X-direction at the center. The plate and the substrate are not considered to have any contact boundary conditions between them and are considered as a single structure for the process of the analysis.

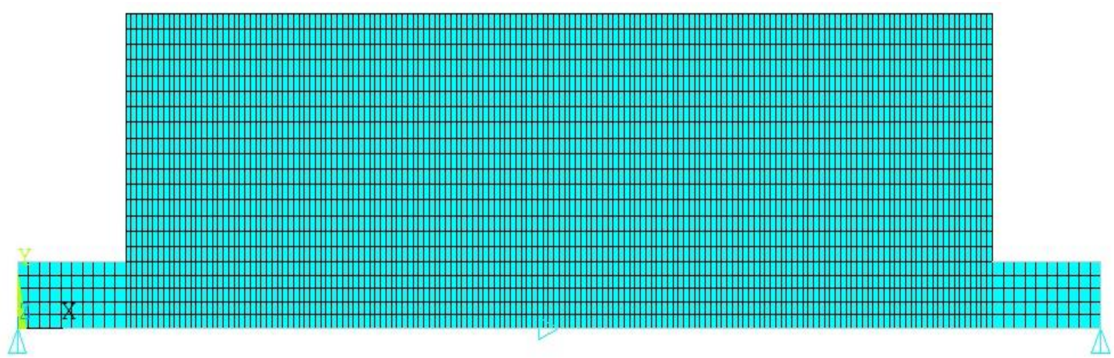

Figure 9: Model of the solid plate build with boundary conditions

To simulate the addition of material during the building of the part, the element "birth and death" technique is employed in ANSYS. The model is initially created with all the nodes and elements. The elements which are going to be added at a later stage are then "killed". To achieve the "element death" effect, the ANSYS program does not actually remove "killed" elements. Instead, it deactivates them by multiplying their stiffness (or conductivity, or other analogous quantity) by a severe reduction factor. This factor is set to 10^{-6} by default, but can be given other values. Element loads associated with deactivated elements are zeroed out of the load vector. Similarly, mass, damping, specific heat, and other such effects are set to zero for deactivated elements. The mass and energy of deactivated elements are not included in the summations over the model. An element's strain is also set to zero as soon as that element is killed.

In a similar manner, when elements are "born," they are not actually added to the model; they are simply reactivated. The elements are initially deactivated, and when they need to be added, are activated at that time. When an element is reactivated, its stiffness, mass, element loads, etc. return to their full original values. Elements are reactivated having no record of strain history (or heat storage, etc.).

A flowchart to describe the simulation process is shown below in Figure 10. The element type and the material properties of the metal are defined in ANSYS. The geometry is then either created in ANSYS or imported from a Solid Modeling software. The model is then meshed creating nodes and elements. Boundary conditions are assigned to the mesh. Initial conditions are attributed to these nodes and elements. A uniform preheat temperature is applied to the substrate. The elements that are not part of the substrate are then killed. The first layer is activated and the moving electron beam is applied as a heat flux load to this layer. When the heat source reaches the end of the layer, the next layer is activated and the moving heat source is applied again to this new layer. This process continues till all the layers have been added. In between layer addition, there may be a portion of time when the beam is not turned on and heat is not being added to the system. This portion of time is referred to as the dwell time between layers and is an important process parameter that needs to be considered during part builds. Once the build is complete, the model enters the cooling phase to bring it to ambient temperature. The built part at this ambient temperature is then analyzed for any distortion.

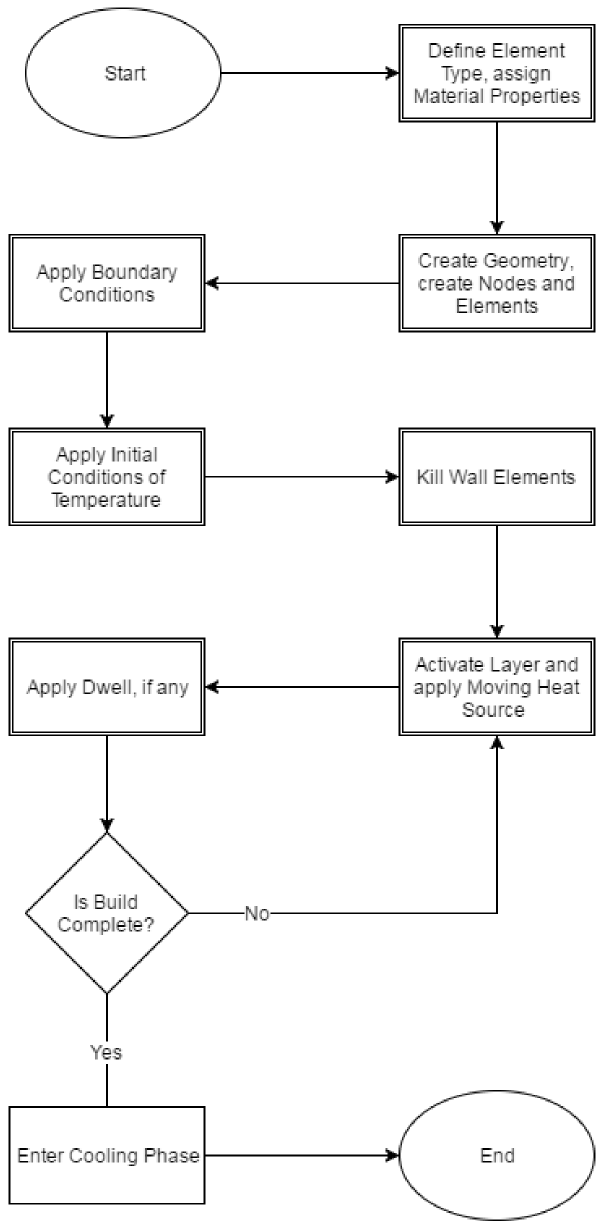

Figure 10: Flowchart of simulation

The moving heat source was assumed to take the shape of a Gaussian distribution. The coupled element PLANE13 used in this analysis can only to be subject to point loads at the nodes or surface loads over the edges. Before the heat flux was added as a load to the mesh, a local coordinate system was defined at the point of application of the heat source. The heat flux value was then calculated at the centroid of every element radiating out of the origin of this local coordinate system until a minimum threshold value of 10^{-5} was obtained. The elements within this region were then considered for load application in the given time step. The load at the centroid for each element was calculated and then equally distributed to its four constituting nodes. The load step was then solved for this value of load. The loads are then removed and the point of application was then moved forward a distance determined by the speed of the beam. The time step was incremented in a similar manner and the process was repeated. During the next load step, some of the elements subjected to loads in the previous load step will still have loads applied to them in the current load step but these loads will have a different load value as their distance from the origin of the local coordinate system will have changed. In this manner, the Gaussian distribution is converted to point loads on the mesh. A fairly refined mesh justifies this approximation.

Five mesh sizes of 10 mm, 6mm, 2.5, 1.25 mm and 0.6 mm were considered as part of a convergence study. For mesh sizes of 1.25 mm 0.6 mm, the maximum computed temperature between these two cases had a difference of less than 4%. So, mesh size of 1.25mm was used to mesh the model to be more computationally efficient.

ANSYS employs the Newton-Raphson approach to solve nonlinear problems. In this approach, the load is subdivided into a series of load increments. The load increments can be applied over several load steps. Before each solution, the Newton-Raphson method evaluates the out-of-balance load vector, which is the difference between the restoring forces (the loads corresponding to the element stresses) and the applied loads. The program then performs a linear solution, using the out-of-balance loads, and checks for convergence. If convergence criteria are not satisfied, the out-of-balance load vector is re-evaluated, the stiffness matrix is updated, and a new solution is obtained. This iterative procedure continues until the problem converges. A number of convergence-enhancement and recovery features, such as line search, automatic load stepping, and bisection, can be activated to help the problem to converge. If convergence cannot be achieved, then the program attempts to solve with a smaller load increment. The ANSYS program gives a number of choices for designating the convergence criteria based on forces, moments, displacements, or rotations, or on any combination of these items. Additionally, each item can have a different convergence tolerance value. For the current analysis, the convergence criteria were based on checking forces and considered a minimum value of 10^{-6}.

A uniform preheat temperature of 700^{o}C was applied to the substrate. The reference temperature and room temperature were considered to be 25^{o}C. Radiation boundary condition was applied to all the free surfaces of the part during the build with an emissivity value of 0.54. After the build was complete, convection was applied to the free surfaces to accelerate the cooling process and bring the part to room temperature at a relatively fast pace. The convection film coefficient was considered to be 18 W/m^{2}/^{o}C.

As mentioned earlier, the aim of these simulations is to predict the effect of process parameters on parts built using EBAM, in order to reduce the amount of distortion in the final part. We varied three process parameters, namely the beam power, the velocity of the beam and the dwell time between layers. The beam powers considered were 6 kW, 7 kW, 8 kW and 9 kW. The dwell times considered were 0 s, 20 s, 40 s and 60 seconds. The four beam velocities considered were 5 mm/s, 8 mm/s, 10 mm/s and 12.7 mm/s. A total of 48 cases were run for various combinations of these above-mentioned parameters and they have been listed in Table 2. The table also shows the maximum distortion as calculated by the model after the part was cooled to room temperature. The simulations took between 30 minutes and 90 minutes when run on a standard desktop computer.

Table 2: List of simulations with computed maximum part distortion after cooling

Sl. No.	Power (kW)	Dwell (seconds)	Speed (mm/s)	Maximum distortion after cooling (mm)
1	6	0	5	10.8
2	6	0	8	6.71
3	6	0	10	6.35
4	6	0	12.7	6.38
5	6	20	5	4.53
6	6	20	8	1.96
7	6	20	10	1.99
8	6	20	12.7	3.64
9	6	40	5	4.74
10	6	40	8	1.38
11	6	40	10	1.62
12	6	40	12.7	3.98
13	6	60	5	5.08
14	6	60	8	0.95
15	6	60	10	2.49
16	6	60	12.7	3.26
17	7	0	5	12.14
18	7	0	8	6.98
19	7	0	10	5.91
20	7	0	12.7	6.29
21	7	20	5	4.03
22	7	20	8	0.7
23	7	20	10	0.97
24	7	20	12.7	1.53
25	7	40	5	3.84
26	7	40	8	0.19
27	7	40	10	0.86
28	7	40	12.7	1.46
29	7	60	5	3.92
30	7	60	8	1.02
31	7	60	10	1.17
32	7	60	12.7	1.93
33	8	0	5	12.9
34	8	0	8	7.07
35	8	20	5	3.77
36	8	20	8	0.51
37	8	40	5	3.36
38	8	40	8	1.51
39	8	60	5	3.58
40	8	60	8	1.98
41	9	0	5	13.64
42	9	0	8	7.18
43	9	20	5	4.34
44	9	20	8	1.35
45	9	40	5	3.11
46	9	40	8	2.41
47	9	60	5	2.99
48	9	60	8	2.87

As an example simulation, Figure 11 shows the predicted temperature contours (^oC) at the completion of the build, which are superimposed on the distorted part shape. For reference, the dashed line shows the initial undeformed part geometry. The upward distortion of the part is clearly evident when compared with this dashed line. The figure also shows the large temperature gradients that occur in the part. Note that the highest temperature is concentrated near the top and final layer of the part immediately after completion of the build. This is expected since the beam passed along the top of the part (from left to right) in the final pass to build the part. For comparison, Figure 12 shows the final distortion of the part after it has returned to room temperature. Note that the temperature distribution is nearly uniform after cooling to room temperature.

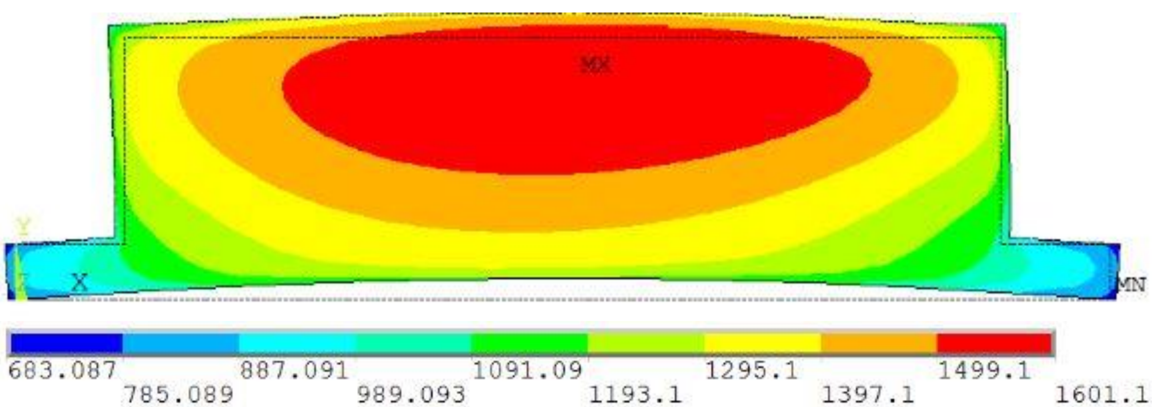

Figure 11: Temperature distribution at completion of build for simulation case of Power = 6 kW, Dwell Time = 20 s and Beam Speed = 12.7 mm/s. Maximum distortion value = 4.5 mm

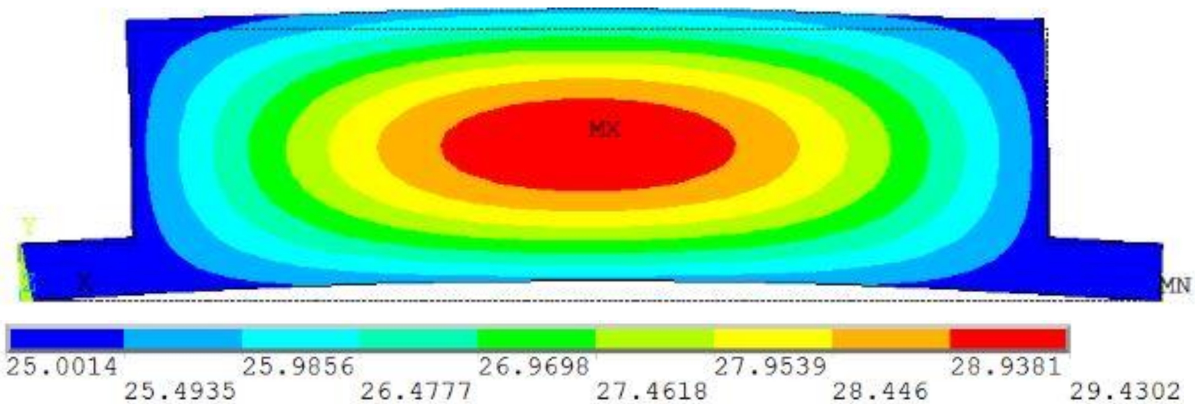

Figure 12: Temperature distribution after part is cooled to ambient temperature for simulation case of Power = 6 kW, Dwell Time = 20 s and Beam Speed = 12.7 mm/s. Maximum distortion value = 3.6 mm

For the same simulation case, Figures 13 and 14 show the variation of displacement and temperature at the node that is located at the midspan and on the top surface of the substrate.

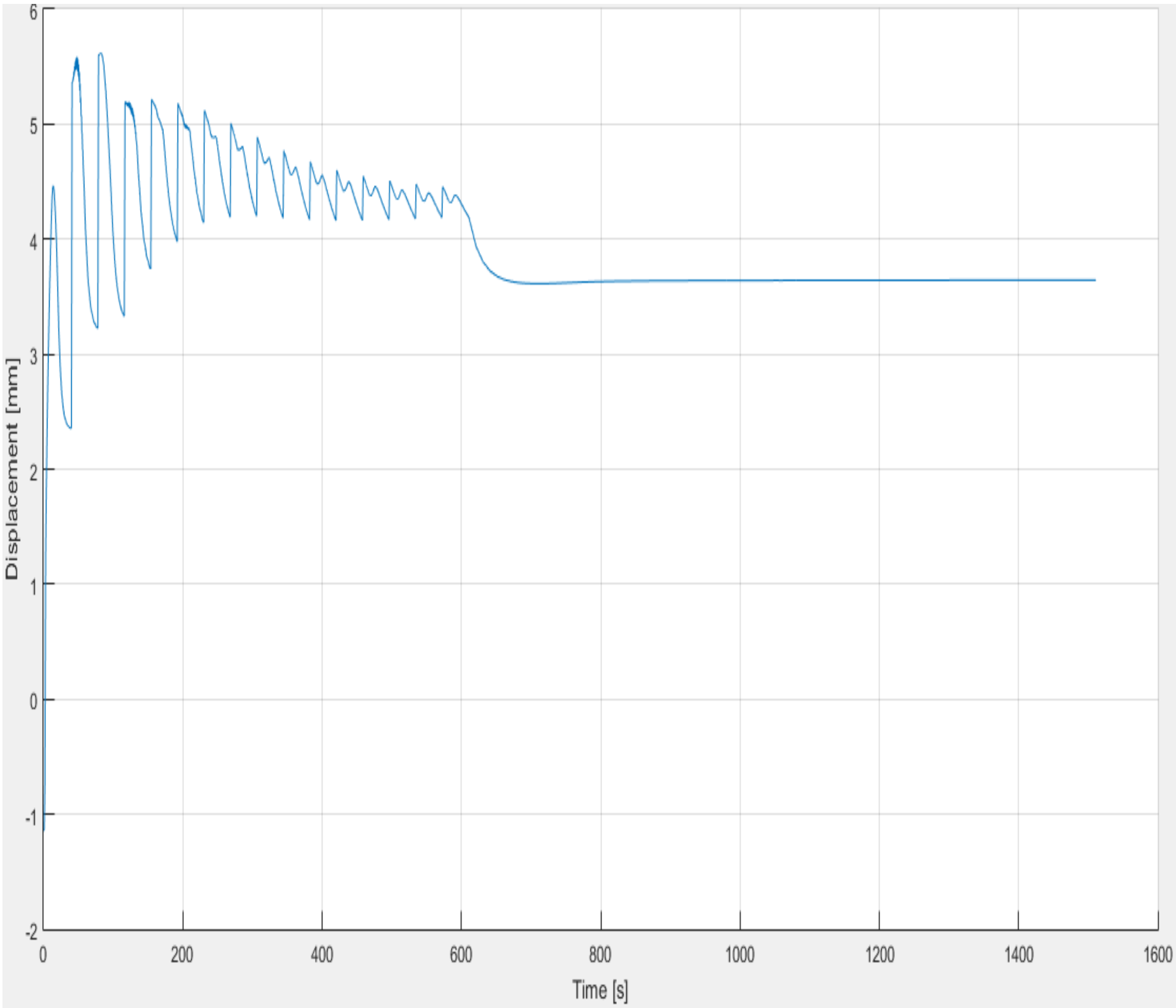

Figure 13: Vertical displacement of node at midspan on top surface of substrate

As shown in Figure 13, the maximum distortion is approximately 5.5 mm. The oscillations in Figure 13 are a result of the material and heat addition during the build. As the layers are built, the heat source moves away from the node under consideration, which explains the decrease in the level of displacement with time. The sudden drop in the displacement around the 600 second mark is a result of the beam being turned off after the completion of the build and the onset of the cooling process. The horizontal portion is the cooling cycle which shows no displacement during that period of time. After this time, the part cools to the ambient temperature. Note that a nodal displacement of approximately 3.6 mm remains which results in the final part distortion.

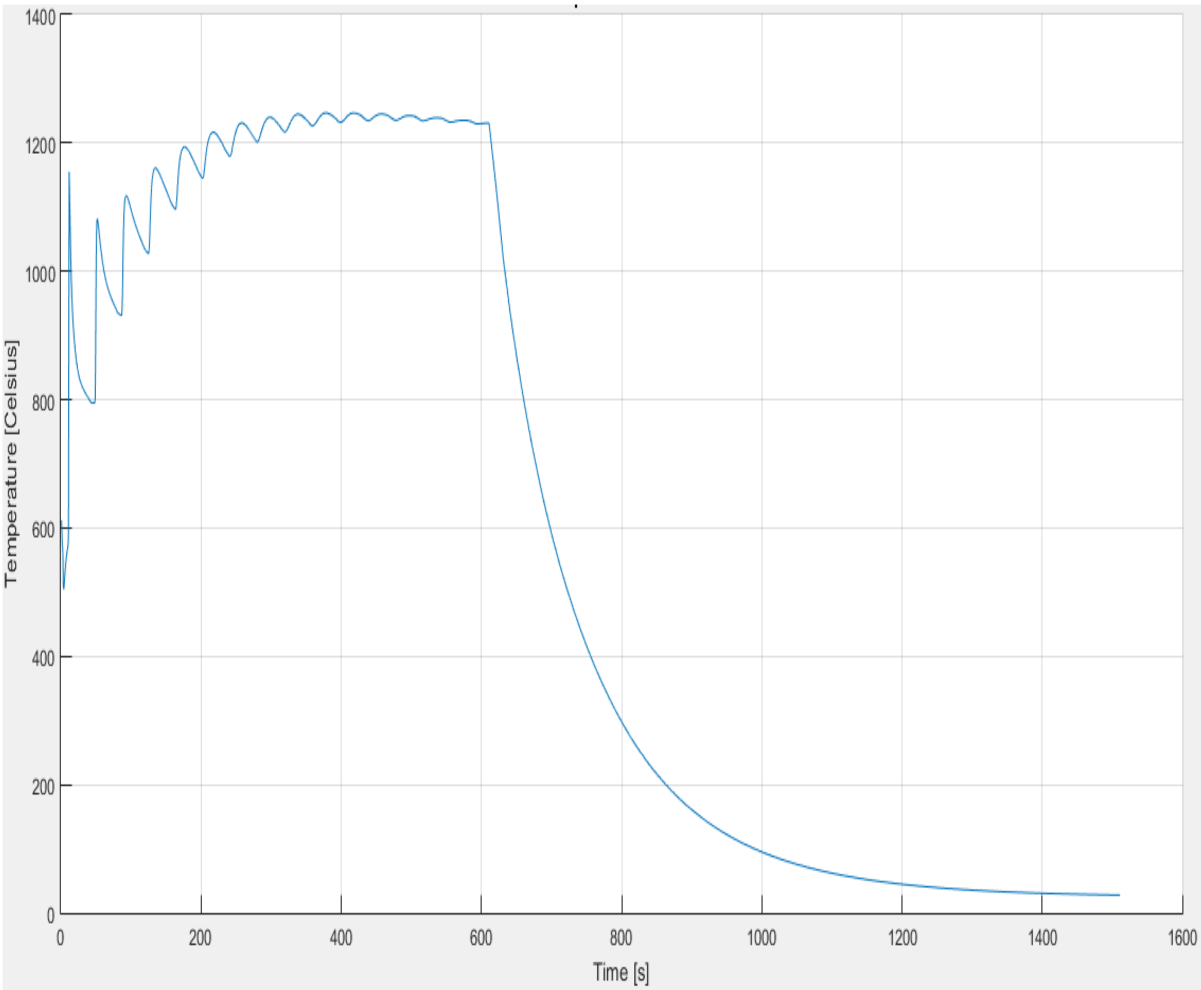

Figure 14: Temperature variation of node at midspan on top surface of substrate

The temperature variation in Figure 14 shows a similar trend. The temperature increases during the layer by layer material addition and tapers off towards the end of the build. The sudden drop in the temperature indicates the beam being turned off and the onset of the cooling cycle.

The distortion levels for the 48 simulation cases were analyzed next to determine the relationship between predicted part distortion and various operating parameters including beam power, dwell time and speed. The distortion shown in the following figures was calculated at the midspan along the top of the plate.

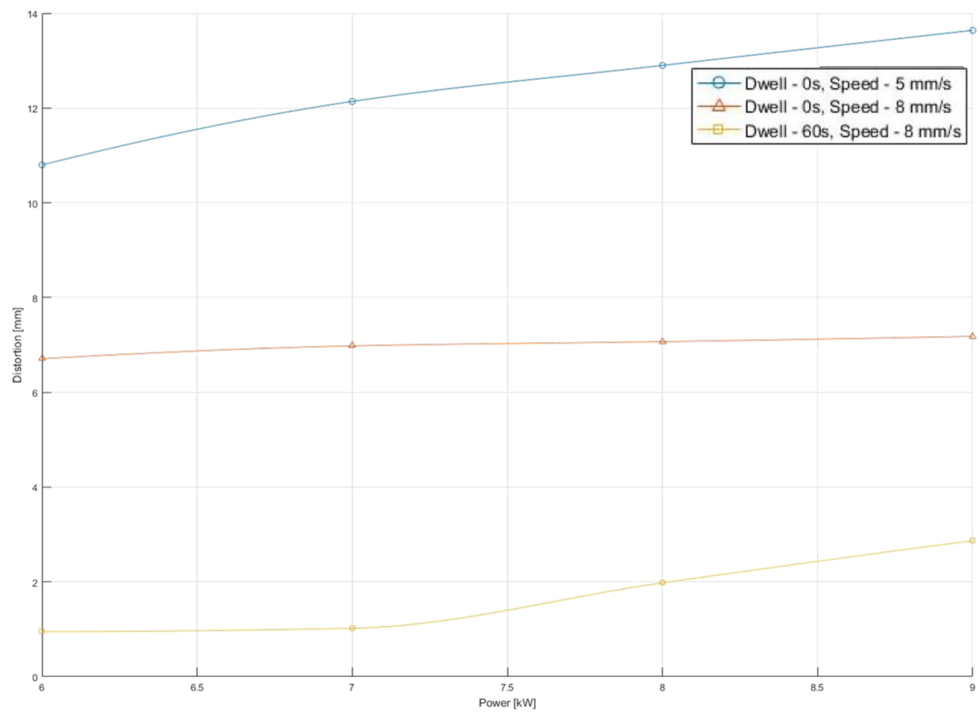

Figure 15: Distortion vs Power

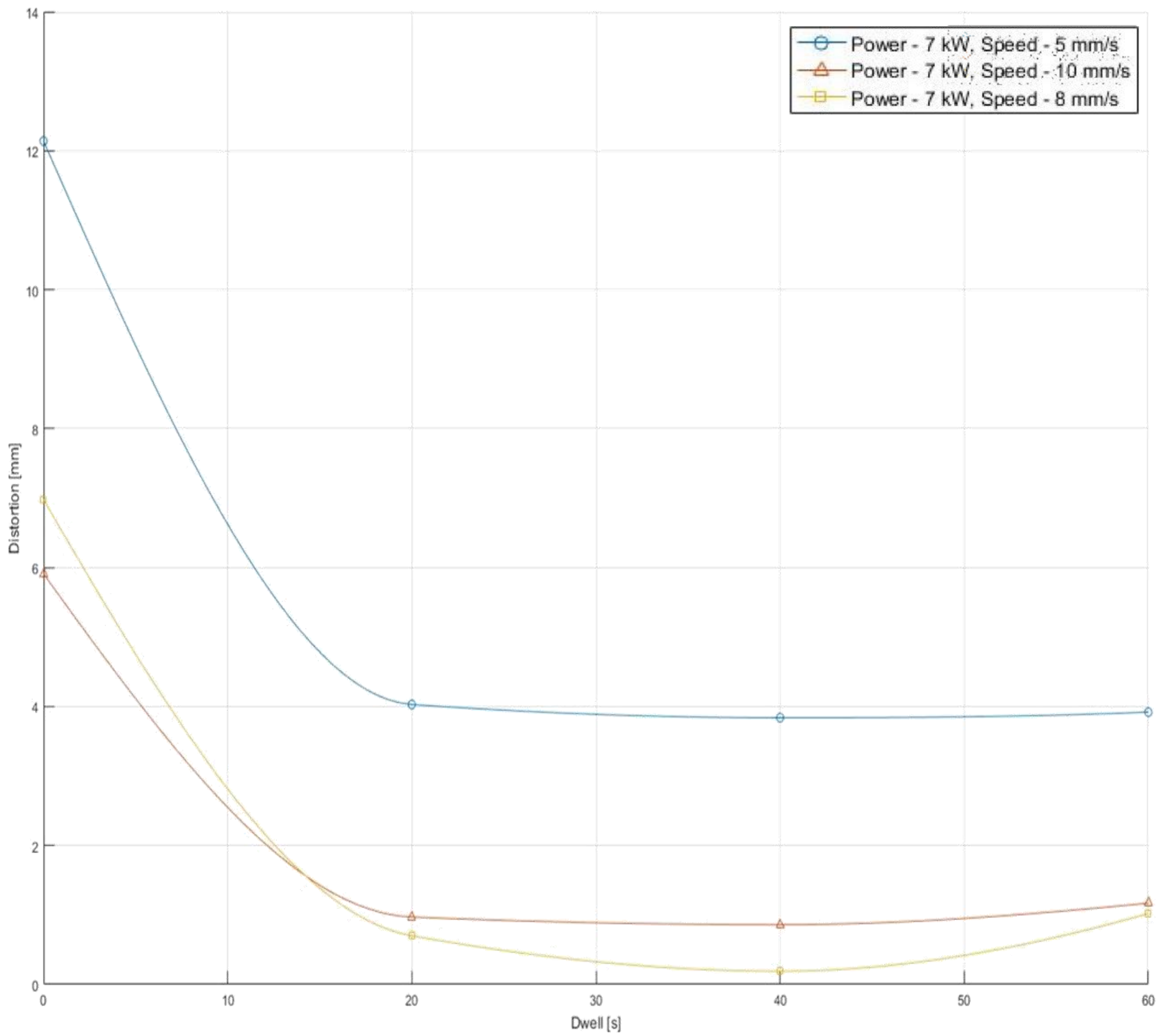

Figure 16: Distortion vs Dwell Time

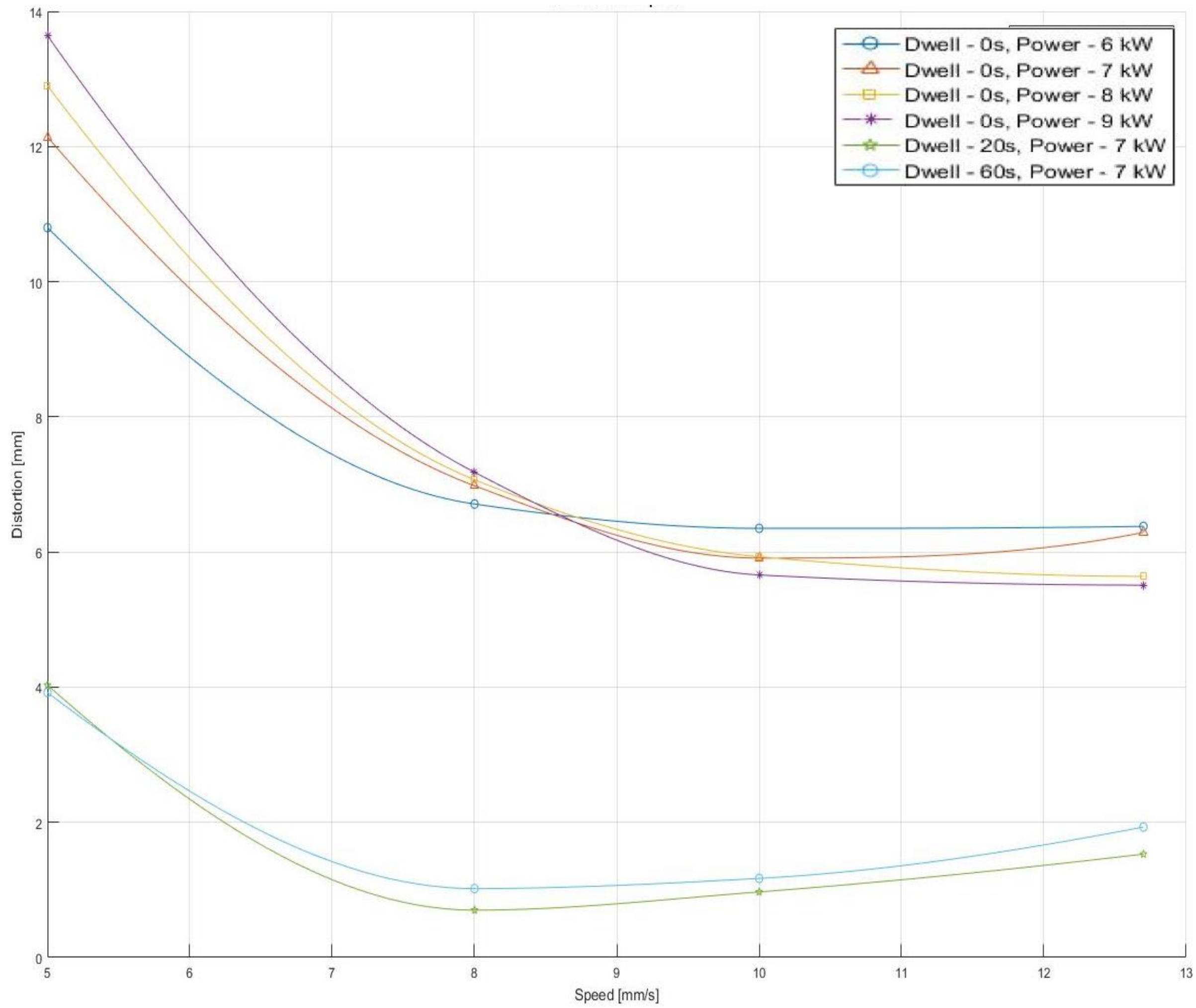

Figure 17: Distortion vs Speed

Figure 15 shows the variation of distortion with beam power. The three curves shown in this figure represent (1) no dwell time and a speed of 5 mm/s, (2) no dwell time and a speed of 8 mm/s, and (3) a dwell time of 60 seconds and speed of 8 mm/s. As expected, the distortion increases with increase in beam power since more heat is being added to the part resulting in larger thermal and strain gradients between layers within the part. The largest distortion occurs for zero dwell time and the lower speed of 5 mm/s because more heat is being added to the part when the beam moves more slowly. In contrast, less heat is imparted at the higher speed of 8 mm/s and the 60 second dwell time. In addition, the larger dwell time allows the heat to be more evenly distributed throughout the part before the next layer is applied.

Figure 16 shows the distortion as a function of dwell time for a given power of 7 kW and 3 speeds of 5 mm/s, 8 mm/s and 10 mm/s. This figure clearly demonstrates the importance of the dwell time in reducing part distortion. The distortion drastically reduces with the addition of any dwell time to the process and gradually tapers out. The absence of dwell time in a process means that layers are continually built without any time for the heat to distribute itself within the part between successive layers. This will result in high thermal gradients within the part which will result in high thermal strains and high distortion levels as shown. With the addition of dwell time to the process, the heat is allowed to diffuse and distribute itself within the part before the next layer is added. This allows for a more uniform temperature increase across the layers which will help with keeping the part distortion low.

Figure 16 also shows a trend of the distortion levels becoming almost the same over a span of dwell time of 20 seconds to 60 seconds. This is an indication that an indefinite increase in dwell time is not going to contribute to keeping the distortion level low. With very large dwell times, the heat is allowed to diffuse within the part and the part may also undergo some amount of cooling and solidification, which can be detrimental to the build process. In such a scenario, when the new layer is added, there is a very large temperature differential at the interface which can manifest itself as higher distortion within the part. Figure 16 also shows a small increase in the distortion level with increase in dwell time for one of the cases shown, suggesting that there is a minimum value of dwell time for a given beam power and speed configuration that can help keep the distortion level to a minimum. By making such a study at the design level, the optimum dwell time can be obtained which will reduce the time spent on building prototypes in a trial and error manner to determine the best dwell time for the part.

Figure 17 shows a variation of the distortion as a function of the beam speed for a given power and dwell time. The top four curves correspond to four beam powers of 6 kW, 7 kW, 8 kW and 9 kW with no dwell time. The lower two curves represent two beam powers and two dwell times of 20 seconds and 60 seconds. The figure shows that with increase in speed of the electron beam, there is reduction in the level of distortion seen in the part. Increasing the beam speed reduces the energy density input in to the part. The beam moves over the part at a pace that does not allow for the heat to penetrate into the layers to the same extent as would be the case for a lower speed. This has been taken into account in the Gaussian heat source model by having the higher velocities penetrate to a smaller extent into the part when compared with a lower velocity. This results in a reduced maximum process temperature, which translates to a lower distortion at the part level. This compares with the study made by Price et al. [44] who studied the effect of the process parameters on the thermal characteristics in EBAM with Ti6Al4V powder. They found that increasing the beam speed reduced the peak temperatures and reduced the melt pool sizes resulting in parts being produced with rougher surfaces and more pore features. Note also that distortion decreases as the dwell time is increased, which is consistent with the previous figure. The lower two curves in this figure also suggest that there is an optimal speed of about 8 mm/s for which the distortion is a minimum.

Besides the plate configuration that has been discussed so far, other geometries were also studied and the final deformed shapes of these geometries have been shown below.

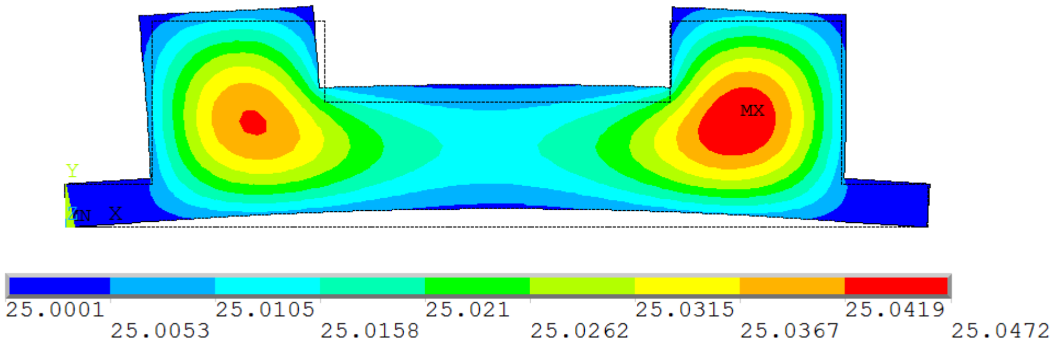

Figure 18: Distorted shape of plate with single slot. Maximum distortion value = 5.5 mm

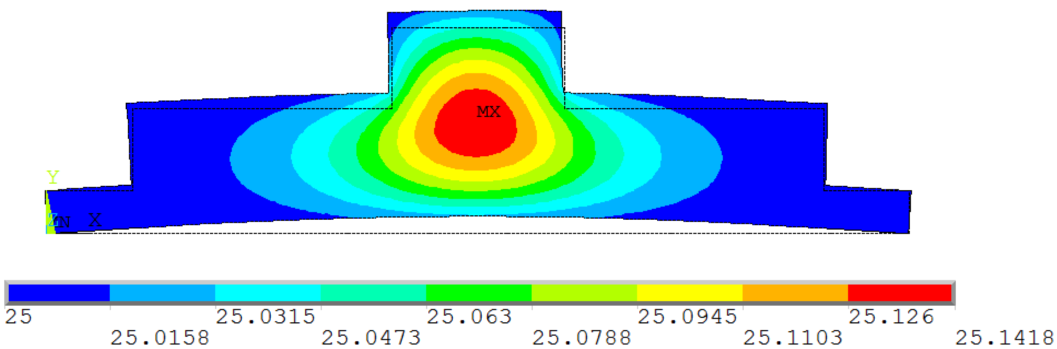

Figure 19: Distorted shape of plate with a step. Maximum distortion value = 5.2 mm

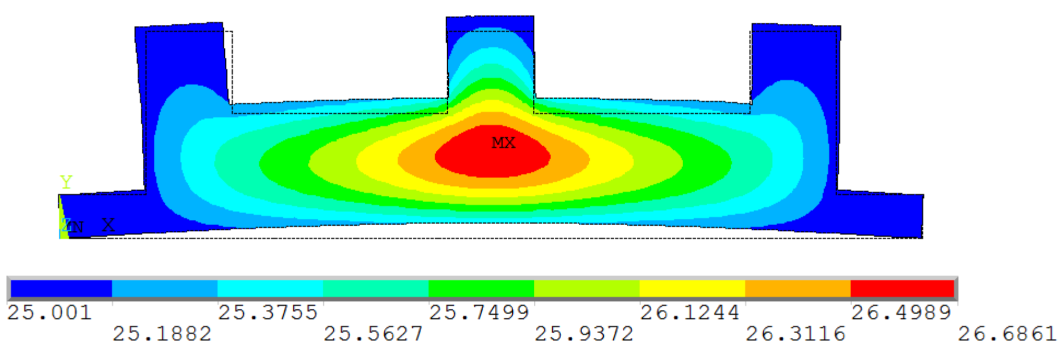

Figure 20: Distorted shape of plate with two slots. Maximum distortion value = 5.9 mm

These geometries were run for the simulation case of power of 6kW, dwell time of 20 seconds and beam speed of 5mm/s. These distorted profiles not only show a distortion along the base but also along the sides and in the cut out portions as well. If these are parts that are going to come into contact with other parts in an assembly, care must be taken to ensure that these parts have minimum distortion at the mating surfaces in order to have proper fits with the joining parts. Some options that can be considered to reduce this distortion are to change the build orientation of the part and simulate it to see if it will result in reduced distortion. However, with a changed orientation, support structures may be needed to be placed where there are overhanging surfaces. A different build configuration for the plate with the longer edge oriented vertically was also studied and is as shown below. The distortion of this new orientation was found to be 4.78 mm. The previous orientation of the longer edge being horizontal yielded a distortion value of 5.81 mm. This clearly suggests that different build orientations can help in reducing distortion in the final part.

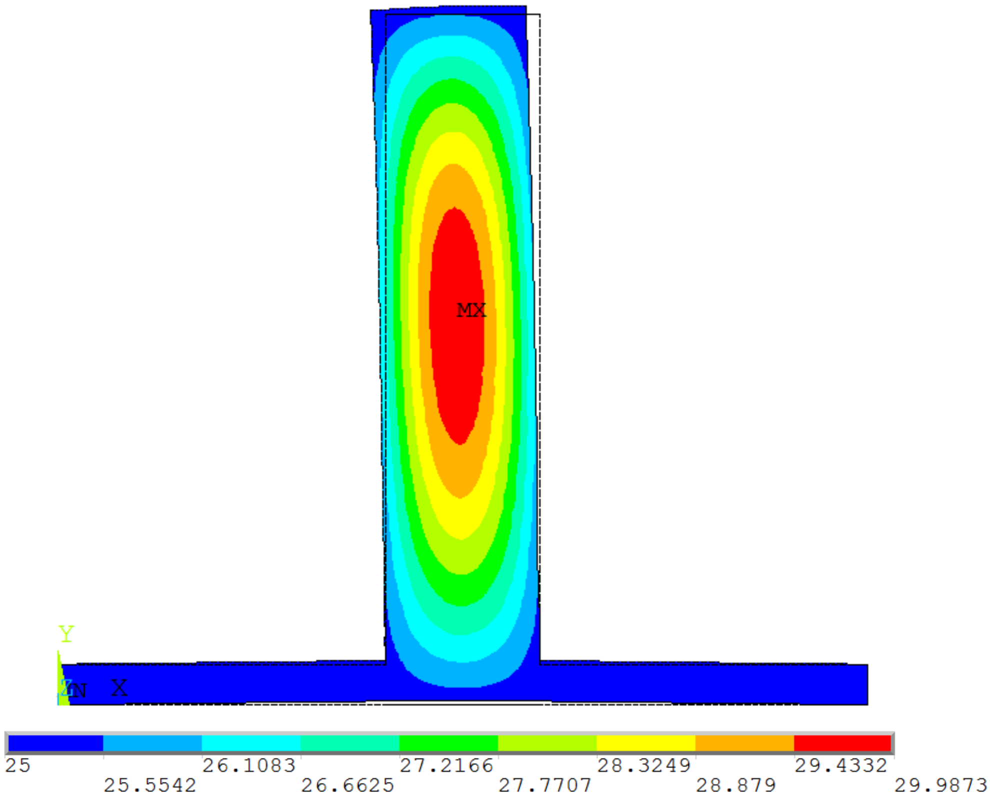

Figure 21: Distortion for solid plate with vertical build orientation

In addition to all these cases, a single case was run with a different value of preheating temperature to see if a reduced preheat temperature would affect the distortion of the part. For a beam power of 9 kW, dwell time of 60 seconds between layers and beam speed of 12.7 mm/s, the simulation was run for a preheat temperature of 200^{o}C. The distortion value obtained was 3.92mm. The same process parameters but with a preheat temperature of 700^{o}C yielded a distortion of 3.63 mm. Thus, this suggests that the preheat temperature is also an important parameter that needs to be considered for its effect on the part distortion.

Thus, we can see that the process parameters of beam power, speed and dwell time are vital to determining the extent of distortion within the final part. By running various combinations of these parameters in such a simulation, the optimum one can be arrived at which will result in minimum distortion within the part for a given build configuration. In addition to these parameters, the build geometry, build orientation and preheating temperature also contribute to the distortion of the part.

5 CONCLUSION AND FUTURE WORK

5.1 Conclusions

A model was developed to assess part distortion as a function process parameters – power, dwell and speed. Distortion values for various combinations of beam power, speed and dwell time for the given part geometry have been reported in this manuscript. Previous studies in metal additive manufacturing described temperature profiles and residual stress patterns encountered in the different AM processes with the help of both simulations and experiments. These simulations were typically decoupled, the thermal models were separate from the mechanical model and were carried out separately with the output of the thermal simulation being used as the input to the mechanical model. The current model incorporates a coupled thermal and mechanical simulation with radiation and convection. A two-dimensional problem was considered in the interests of computation efficiency. This model can be used as a design tool as it gives a general idea into the physics of the problem and can be utilized for design purposes.

An extensive literature review was performed to determine the work that was already done in this field. Over three hundred papers and articles were reviewed. This literature review also helped in obtaining the temperature dependent properties of Ti6Al4V. These properties are not readily available, especially at the higher temperatures. During the course of the research, the temperature dependent physical properties of Ti6Al4V were obtained for a range of temperatures from ambient temperature to a little beyond its melting point. However, the mechanical properties at temperatures beyond 600^{o}C were not found and hence, suitable approximations for these properties were obtained from the literature. Unfortunately, ANSYS has a limit of six temperatures when defining the plastic behavior of the material and hence, only the properties at these temperatures have been reported in this manuscript and used in the model. A different finite element code with more extensive applications can be considered to take all these properties into account.

Even though the model was two-dimensional, this model provided a good understanding of the physics of what is actually happening in this problem. The approaches of the moving heat source described as a Gaussian distribution and birth and death technique of activating and deactivating elements used in this model helped to capture realistically the physics of the problem. The heat source being input as a heat flux as opposed to a temperature loading further contributes to this approach. The coupled element employed helped to capture both temperature and mechanical effects within a single simulation. All these factors contribute to the model for simulating a realistic approach to describe the physics of the additive manufacturing process.

5.2 Future Work

Future work in this area of research can involve expanding this model to three dimensions to simulate an actual part. This model can then be used to obtain values of the process parameters with which experiments can be carried out. More extensive research can be carried out into the properties of the materials being used in AM processes to better define their behavior at the elevated temperatures experienced in these processes. Future models can then account for latent heat of fusion and change of phase. Research can be conducted to develop temperature-dependent material properties for other materials. Different plasticity models can be explored to more accurately predict part distortion. The effect of preheat temperature, build orientation and different build geometries on the distortion of the part were also analyzed in this study. These parameters as well as scan patterns can be studied more extensively to determine the extent of their contribution to part distortion.

REFERENCES

[1] D. Rosenthal. The theory of moving sources of heat and its application to metal treatments. *Transactions of the ASME 68*pp. 849-866, 1946.

[2] E. Friedman. Thermomechanical analysis of the welding process using the finite element method. *Transactions of the ASME. Series J, Journal of Pressure Vessel Technology 97(3),* pp. 206-13, 1975.

[3] J. Goldak, A. Chakravarti and M. Bibby. New finite element model for welding heat sources. *Metallurgical Transactions. B, Process Metallurgy 15 B(2),* pp. 299-305, 1984.

[4] N. T. Nguyen, A. Ohta, K. Matsuoka, N. Suzuki and Y. Maeda. Analytical solutions for transient temperature of semi-infinite body subjected to 3-D moving heat sources. *Weld J (Miami Fla) 78(8),* pp. 265-s-274-s, 1999.

[5] A. M. Deus and J. Mazumder. Three-dimensional finite element models for the calculation of temperature and residual stress fields in laser cladding. Presented at ICALEO 2006 - 25th International Congress on Applications of Laser and Electro-Optics, October 30, 2006 - November 2, 2006.

[6] E. Toyserkani, A. Khajepour and S. Corbin. 3-D finite element modeling of laser cladding by powder injection: Effects of laser pulse shaping on the process. *Optics and Lasers in Engineering 41(6),* pp. 849-867, 2004.

[7] N. Contuzzi, S. L. Campanelli and A. D. Ludovico. 3D finite element analysis in the selective laser melting process. *International Journal of Simulation Modelling 10(3),* pp. 113-21, 2011.

[8] M. Picasso, C. F. Marsden, J. -. Wagniere, A. Frenk and M. Rappaz. A simple but realistic model for laser cladding. *Metallurgical and Materials Transactions B (Process Metallurgy and Materials Processing Science) 25B(2),* pp. 281-91, 1994.

[9] V. M. Weerasinghe and W. M. Steen. Computer simulation model for laser cladding. Presented at Transport Phenomena in Materials Processing. Presented at the Winter Annual Meeting of the American Society of Mechanical Engineers, 1983.

[10] A. F. A. Hoadley and M. Rappaz. A thermal model of laser cladding by powder injection. *Metallurgical Transactions B (Process Metallurgy) 23B(5),* pp. 631-42, 1992.

[11] G. Zhao, C. Cho and J. Kim. Application of 3-D finite element method using lagrangian formulation to dilution control in laser cladding process. *Int. J. Mech. Sci. 45(5),* pp. 777-796, 2003.

[12] A. Kar and J. Mazumder. Extended solid solution and nonequilibrium phase diagram for dni-al alloy formed during laser cladding. *Metallurgical Transactions A (Physical Metallurgy and Materials Science) 20A(3),* pp. 363-71, 1989.

[13] A. Vasinonta, J. L. Beuth and M. Griffith. Process maps for predicting residual stress and melt pool size in the laser-based fabrication of thin-walled structures. *Transactions of the ASME. Journal of Manufacturing Science and Engineering 129(1),* pp. 101-9, 2007.

[14] A. H. Nickel, D. M. Barnett and F. B. Prinz. Thermal stresses and deposition patterns in layered manufacturing. Presented at Micromechanics and Micromechanisms of Deformation and Fracture: In Honor of Professor Ali S Argon, 2001.

[15] M. Labudovic, D. Hu and R. Kovacevic. A three dimensional model for direct laser metal powder deposition and rapid prototyping. *J. Mater. Sci. 38(1),* pp. 35-49, 2003.

[16] N. N'Dri, H. -. Mindt, B. Shula, M. Megahed, A. Peralta, P. Kantzos, J. Neumann and The Minerals,Metals & Materials Society. "DMLS process modelling & validation," in *TMS2015 Supplemental Proceedings*, 2015.

[17] R. Cottam, K. Thorogood, Q. Lui, Y. Wong and M. Brandt. The effect of laser cladding deposition rate on residual stress formation in ti-6Al-4V clad layers. Presented at 1st International Conference on Powder Processing, Consolidation and Metallurgy of Titanium, December 4, 2011 - December 7, 2011.

[18] I. A. Roberts, C. J. Wang, M. Stanford, K. A. Kibble and D. J. Mynors. Experimental and numerical analysis of residual stresses in additive layer manufacturing by laser melting of metal powders. *Key Eng Mat 450*pp. 461-5, 2011.

[19] M. Matsumoto, M. Shiomi, K. Osakada and F. Abe. Finite element analysis of single layer forming on metallic powder bed in rapid prototyping by selective laser processing. *Int. J. Mach. Tools Manuf. 42(1),* pp. 61-67, 2002.

[20] D. Moser, S. Fish, J. Beaman and J. Murthy. Multi-layer computational modeling of selective laser sintering processes. Presented at ASME 2014 International Mechanical Engineering Congress and Exposition, IMECE 2014, November 14, 2014 - November 20, 2014.

[21] J. R. Cheng. Numerical simulation of laser powder deposition for TC15 titanium alloy brick parts. *Materials Research Innovations 18*pp. 4-940, 2014.

[22] P. Mercelis and J. -. Kruth. Residual stresses in selective laser sintering and selective laser melting. *Rapid Prototyping Journal 12(5),* pp. 254-65, 2006.

[23] K. Dai and L. Shaw. Thermal and stress modeling of multi-material laser processing. *Acta Materialia 49(20),* pp. 4171-81, 2001.

[24] C. Li, C. H. Fu, Y. B. Guo and F. Z. Fang. Fast prediction and validation of part distortion in selective laser melting. *Procedia Manufacturing 1*pp. 355-65, 2015.

[25] D. Buchbinder, W. Meiners, N. Pirch, K. Wissenbach and J. Schrage. Investigation on reducing distortion by preheating during manufacture of aluminum components using selective laser melting. *J. Laser Appl. 26(1),* 2014.

[26] R. Paul, S. Anand and F. Gerner. Effect of thermal deformation on part errors in metal powder based additive manufacturing processes. *J. Manuf. Sci. Eng. Trans. ASME 136(3),* 2014.

[27] S. Marimuthu, D. Clark, J. Allen, A. M. Kamara, P. Mativenga, L. Li and R. Scudamore. Finite element modelling of substrate thermal distortion in direct laser additive manufacture of an aero-engine component. *Proc. Inst. Mech. Eng. Part C 227(9),* pp. 1987-1999, 2013.

[28] L. Papadakis, A. Loizou, J. Risse and J. Schrage. Numerical computation of component shape distortion manufactured by selective laser melting. Presented at 1st International Conference on Manufacture of Lightweight Components, ManuLight2014, April 3, 2014 - April 4, 2014.

[29] W. Yan, Z. Yue and J. Zhang. Study on the residual stress and warping of stiffened panel produced by electron beam freeform fabrication. *Materials and Design 89*pp. 1205-1212, 2016.

[30] E. R. Denlinger, J. Irwin and P. Michaleris. Thermomechanical modeling of additive manufacturing large parts. *J. Manuf. Sci. Eng. Trans. ASME 136(6),* 2014.

[31] B. Cheng, P. Lu and K. Chou. Thermomechanical investigation of overhang fabrications in electron beam additive manufacturing. Presented at ASME 2014 International Manufacturing Science and Engineering Conference, MSEC 2014 Collocated with the JSME 2014 International Conference on Materials and Processing and the 42nd North American Manufacturing Research Conference, June 9, 2014 - June 13, 2014.

[32] P. Lacki and K. Adamus. Numerical simulation of the electron beam welding process. *Comput. Struct. 89(11-12),* pp. 977-85, 2011.

[33] E. R. Denlinger, J. C. Heigel and P. Michaleris. Residual stress and distortion modeling of electron beam direct manufacturing ti-6Al-4V. *Proceedings of the Institution of Mechanical Engineers, Part B (Journal of Engineering Manufacture) 229(10),* pp. 1803-13, 2015.

[34] N. Shen and K. Chou. Simulations of thermo-mechanical characteristics in electron beam additive manufacturing. Presented at ASME 2012 International Mechanical Engineering Congress and Exposition, IMECE 2012, November 9, 2012 - November 15, 2012.

[35] M. Zäh, S. Lutzmann, M. Kahnert and F. Walchshäusl. Determination of process parameters for electron beam sintering (EBS). Presented at Excerpt from the Proceedings of the COMSOL Conference Hannover, 2008.

[36] N. W. Klingbeil, J. L. Beuth, R. K. Chin and C. H. Amon. Residual stress-induced warping in direct metal solid freeform fabrication. *Int. J. Mech. Sci. 44(1),* pp. 57-77, 2002.

[37] B. N. Turner and S. A. Gold. A review of melt extrusion additive manufacturing processes: II. materials, dimensional accuracy, and surface roughness. *Rapid Prototyping Journal 21(3),* pp. 250-261, 2015.

[38] *Materials Properties Handbook Electronic Resource] : Titanium Alloys* 1994.

[39] *Atlas of Stress-Strain Curves* 2002.

[40] *Military Handbook - MIL-HDBK-5H Electronic Resource]: Metallic Materials and Elements for Aerospace Vehicle Structures (Knovel Interactive Edition)* 2003A.

[41] K. C. A. Mills. *Recommended Values of Thermophysical Properties for Selected Commercial Alloys Electronic Resource]* 2002.

[42] A. Anca, V. D. Fachinotti, G. Escobar-Palafox and A. Cardona. Computational modelling of shaped metal deposition. *Int J Numer Methods Eng 85(1),* pp. 84-106, 2011.

[43] B. Chen. *Prediction of Heating Induced Temperature Fields and Distortions in Steel Plates* Technical University of Lisbon, 2011.

[44] S. Price, B. Cheng, J. Lydon, K. Cooper and K. Chou. On process temperature in powder-bed electron beam additive manufacturing: Process parameter effects. *Journal of Manufacturing Science and Engineering-Transactions of the Asme 136(6),* pp. 61019, 2014.

[45] J. M. Gere and S. P. Timoshenko. *Mechanics of Materials* 1997.